JOURNAL OF GEOPHYSICAL RESEARCH, VOL. 87, NO. B8, PAGES 6906-6918, AUGUST 10, 1982

MODELING OF MICROSEISMIC SURFACE WAVE SOURCES

Rüdiger Szelwis

Institut für Geophysik, Universität Hamburg, Hamburg, FRG

Abstract. In a recent paper by Szelwis (1980) microseismic surface waves were inverted with respect to modal contribution and direction of approach. Array cross spectra of two observational runs were analyzed. The microseismic energy peaking in a frequency range of about 0.13 Hz to 0.17 Hz was found to be essentially transported in the two lowest Rayleigh modes and the fundamental Love mode, approaching from one directional interval. In the present paper, the direction mode structure is related to the sources of microseisms. The Rayleigh waves are attributed to ocean wave interactions at the Norwegian coast. This is verified on the basis of Hasselmann's (1963) theoretical concept of the generation of microseisms, by estimating the corresponding source spectrum in two different ways. On the one hand, it is computed from the mode structure observed and a model of the wave-carrying medium including refraction and attenuation. On the other hand, it is computed from a model of the ocean wave field subject to specular reflection from a planar coast. The ocean wave model is taken from sea wave generation research, the input parameters--wind velocity and fetch--are read from the weather charts. The two source spectrum estimates agree within reasonable limits of the model parameters, thus supporting the assumed Rayleigh wave generation mechanism. The Love waves appear to be coupled to the Rayleigh waves, as (1) both wave types approach from the same directions, and (2) their modal spectra relative to the subsurface transfer functions show a high frequency-by-frequency correlation, implying corresponding peak frequencies. A common origin, examined in terms of the spectra of one source, is not compatible with the underlying models.

Introduction

Since Bertelli [1872], who appears to be the first scientific investigator of microseisms, the nature and origin of oscillations in the frequency band 0.05 Hz to 0.5 Hz has attracted considerable attention. Large amounts of data have been collected but could not be quantitatively explained for a long time, owing to the linear and deterministic concepts applied.

Definitive improvement of the structural analysis has been achieved by interpreting microseisms in terms of a (stationary and homogeneous) random process. Observations with seismometer arrays have revealed the dominance of Rayleigh and Love waves, while body waves, which have also been recorded at LASA (Large Aperture Seismic Array, Montana), are relatively unimportant at near-coastal stations [Gutenberg and Benioff, 1956; Toksöz and Lacoss, 1968; Lacoss et al., 1969; Haubrich and McCamy, 1969; Bungum et al., 1971].

Most investigations devoted to the generation problem have revealed correlations between microseisms and ocean wave activity either in coastal regions or in the centers of atmospheric depressions. In particular, 1:1 or 2:1 correspondences between peak frequencies of microseismic and sea surface wave spectra have led to a definition of primary frequency (PF) and double frequency (DF) microseisms [Wiechert, 1904; Banerji, 1930; Gherzi, 1930; Jung, 1934; Bernard, 1941; Gutenberg, 1947, 1953; Båth, 1949; Darbyshire, 1950; Oliver and Ewing, 1957; Haubrich et al., 1963; Hinde and Gaunt, 1966; Darbyshire and Okeke, 1969; Haubrich and McCamy, 1969].

In a theoretical approach made by Press and Ewing [1948], microseisms are associated with stationary values of the group velocity ('Airy phases') of a layer system. However, this is not consistent with data observed.

Miche [1944] gave a physical explanation of microseism generation by the nonlinear interaction of standing water waves, equivalent to a fluctuating pressure independent of depth. The mechanism underlies Longuet-Higgins' [1950] theory of the origin of (DF) microseisms, and is known today as the 'Longuet-Higgins effect.'

Hasselmann [1963] has developed a general statistical approach to the generation problem. He found that (1) DF microseisms may be generated by nearly oppositely traveling water wave components, which means that no standing waves are necessary; (2) PF microseisms originate from nonlinear interaction between sea surface waves and the sea bottom topography; and (3) atmospheric turbulence has a negligible influence upon microseism generation. These theoretical results were used to explain measurements of PF and DF microseisms made by Haubrich et al. [1963], and good agreement was found.

Although straightforward, Hasselmann's results relating the observable spectra of microseisms to their source spectra have not since been applied. Present knowledge may be characterized by the results of Haubrich and McCamy [1969] obtained at LASA. Part of their findings are cited here: (1) PF microseismic surface waves (0.06 Hz to 0.09 Hz) can be explained by ocean waves near coasts; (2) DF microseismic surface waves (0.12 Hz to 0.16 Hz) come mostly from coastline areas. The authors conclude that coastal reflection of ocean waves is responsible for most DF seismic generation; (3) horizontal motion consists of both Love and Rayleigh modes below 0.2 Hz. At any given time, Love waves are likely to come from the same directions as Rayleigh waves, suggesting that Love wave noise originates near coastlines. The authors do not specify surface wave source energies. These require separation of the wave field into subsurface and source properties.

Paper number 2B0554.
0148-0227/82/002B-0554$05.00

Outline of the Procedure

In this paper, observed microseismic surface waves are related quantitatively to their dominant sources. The theoretical concept is adopted from Hasselmann's [1963] 'A statistical analysis of the generation of microseisms'—referred to as paper 1 in the text. According to Hasselmann, microseisms originate from random pressure fields at the earth's surface, owing to resonance between pressure components and the system of elastic layers. The system response consists of free Rayleigh modes. Their space-time dependence is governed by the energy transport equation relating modal spectra, equivalent pressure spectrum of the source (= 'source spectrum'), and transfer functions of the wave guide. A solution of this equation is used here to obtain source spectrum estimates from microseismic observations.

Observational data are taken from a recent paper [Szelwis, 1980]—referred to as paper 2 in the text—which analyzes microseismic surface waves with respect to modal contribution and direction of approach. The two observational runs analyzed contain Rayleigh and Love waves. Both wave types approach from the same directions, and their fundamental mode spectra relative to the subsurface transfer functions ('transfer coefficients') show a high frequency-by-frequency correlation, implying corresponding peak frequencies. The experimental evidence is interpreted as follows.

1. The Rayleigh wave component is attributed to interaction of ocean waves reflected from the Norwegian coast. The interpretation is tested by estimating the corresponding source spectrum from the Rayleigh mode structure, and, independently, from a spectral model of the coastal ocean surface wave field.
2. On the basis of the consistent Rayleigh wave source model, the coupling between Love and Rayleigh waves is examined with respect to a common origin. A criterion is the degree of correlation between hypothetical Love wave source spectra and the Rayleigh wave source spectrum, as against that between the corresponding transfer coefficients.

Model of Microseismic Wave Propagation

According to the concept developed in paper 1, the dependence between microseismic (Rayleigh) waves and their sources is governed by the energy transport equation. A straightforward solution of this equation follows under the assumptions that (1) the source spectrum is constant within a 'source area' and zero outside, and (2) lateral refraction is negligible. Then the solution can be written in the simple form

$$\tilde{F}_i^{(n)}(f,\ \theta) = \Delta(\theta)\tilde{T}_i^{(n)} S(\underline{k}_n,\ -f) \qquad (1)$$

(cf.(1.15) of paper 1), where $\tilde{F}_i^{(n)}(f,\ \theta)$ = density with respect to frequency f, and direction of approach θ, of a linear field variable; $\tilde{T}_i^{(n)}$ = transfer function of the laterally homogeneous wave guide; $\Delta(\theta)$ = linear extension of the source area in θ direction; $S(\underline{k}_n,\ -f)$ = source spectrum, generally dependent upon frequency and horizontal wave number vector $\underline{k}_n$. Index n refers to the nth mode, and i refers to the Cartesian component of the field variable, for example, surface displacement velocity.

In the case of a sufficiently distant source, where the wave energy approaches from a narrow directional interval of width $d\theta$, equation (1) is replaced by

$$\tilde{F}_i^{(n)}(f,\ \theta)d\theta \approx P_i^{(n)}(f) = \frac{A}{R}\tilde{T}_i^{(n)} S(\underline{k}_n,\ -f) \qquad (2)$$

$P_i^{(n)}(f)$ = spectral density; A = source area, defined by $A = R\ \Delta(\theta)d\theta$ with R = source distance.

Equation (2) may be generalized to include refraction. Assume the subsurface structure to be defined by two individual systems of laterally homogeneous layers for the source and recording areas, both connected by a zone of gradual transition. The transition zone is formally defined by assuming constant modal energy density with respect to the horizontal wave number vector, or in terms of f and θ,

$$c_r^{(n)} v_r^{(n)} \tilde{F}_{e,r}^{(n)}(f,\ \theta_r) = c_s^{(n)} v_s^{(n)} \tilde{F}_{e,s}^{(n)}(f,\ \theta) \qquad (3)$$

where indices e, r, s refer to energy, recording area, and source area, and $c^{(n)}$ = phase velocity, $v^{(n)}$ = group velocity. This paper takes into account narrow-beam incidence and assumes parallel depth contours of the transitional layering, so that Snell's law is applicable in the form

$$\frac{\sin\alpha_r}{\sin\alpha} = \frac{c_r^{(n)}}{c_s^{(n)}}$$

where α and α_r are angles of the seismic rays relative to the contour normal, before and after refraction. Then, using $\alpha + \theta = \alpha_r + \theta_r = \nu$, where ν is the angle of the contour normal relative to the underlying coordinate system, equations (3) and (1) combined yield

$$P_i^{(n)}(f) = \frac{A}{R}\tilde{T}_{i,eff}^{(n)} S(\underline{k}_n,\ -f) \qquad (4)$$

where

$$\tilde{T}_{i,eff}^{(n)} = \frac{\cos(\nu - \theta)\, v_s^{(n)}}{\cos(\nu - \theta_r) v_r^{(n)}} \frac{\tilde{T}_{e,s}^{(n)}}{\tilde{T}_{e,r}^{(n)}} \tilde{T}_{i,r}^{(n)}$$

$$\left|\nu - \theta_r\right| < \frac{\pi}{2}$$

The latter inequality ensures that θ does not exceed the critical angle, defined by $\cos(\nu - \theta_r) = 0$. Equation (4) gives the modal spectral density of a field component in terms of the 'refractive model.' If source and recording areas are represented by the same system of layers, equation (4) obviously reduces to equation (2).

The model of the subsurface structure may be generalized further by accounting for linear attenuation. In real structures, particularly over large distances, wave propagation is generally subject to considerable attenuation losses due to elastic scattering or inelasticity. The standard measure of the combined effects is the dimensionless quality parameter Q. Attenuation measurements by spatial surface wave observations provide the attenuation coefficient $\gamma(f)$, which determines the amount of exponential amplitude decay. Correspondingly, a damping factor is introduced into equation (4) to yield

$$P_i^{(n)}(f) = \frac{A}{R}\tilde{T}_{i,eff}^{(n)} \exp\left[-2\gamma^{(n)}(f)R\right] S(\underline{k}_n, -f) \quad (5)$$

where

$$\gamma^{(n)}(f) = \frac{\pi f}{v^{(n)}Q}$$

and

$$v^{(n)} \equiv \frac{1}{2}(v_s^{(n)} + v_r^{(n)})$$

Mode Direction Structure

Paper 2 presents microseismic observations from a three-station seismometer array, each station consisting of three seismometers for the ground velocity components. By inversion of the array cross spectra, mode structure and azimuth of the surface waves are determined. The analysis is based on a model of the directional frequency spectrum given by

$$\tilde{F}_i^{(n)}(f, \theta) = E^{(n)}(f)\, T_i^{(n)}\, \sigma(\theta) \quad (6)$$

leading to the following representation of the spectral density

$$P_i^{(n)}(f) = E^{(n)}(f) \int_{-\pi}^{\pi} T_i^{(n)}\, \sigma(\theta) d\theta \quad (7)$$

$E^{(n)}(f)$ = transfer coefficient, and $\sigma(\theta)$ = normalized directional distribution. The local transfer functions of equations (6) or (7) are related to those of the former equations by

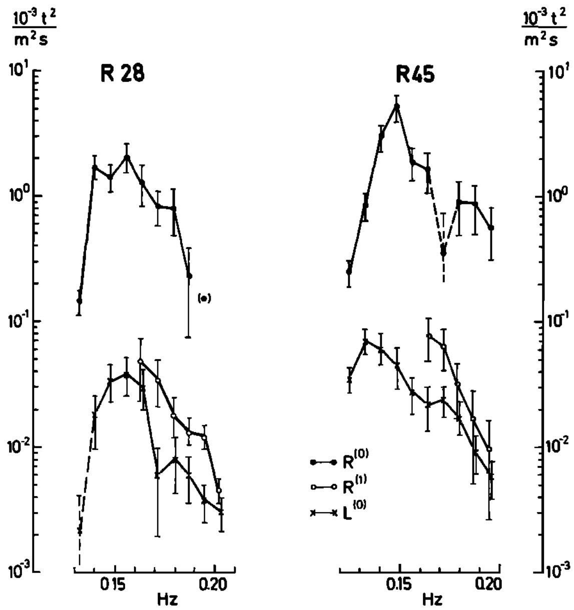

Fig. 1. Transfer coefficients with 90% confidence intervals of the two lowest Rayleigh modes, $R^{(0)}$, $R^{(1)}$, and of the fundamental Love mode, $L^{(0)}$, estimated from array cross spectra of two observational runs, R28 and R45, corresponding to September 16, 1975, 18 h, and September 22, 1975, 13 h (adopted from paper 2).

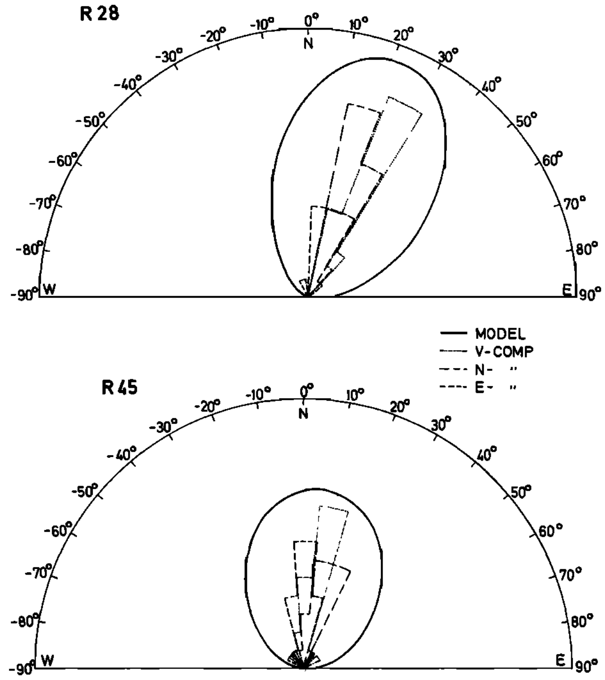

Fig. 2. Microseismic directions. The sectors represent histograms of componental 'tripartite' directions, with class intervals of 10° and relative units of radius length, agreeing for both runs. The smooth curve gives the model estimate.

$$\frac{\tilde{T}_i^{(n)}}{T_i^{(n)}} = \frac{k_n}{(v^{(n)})^2}$$

Two observational runs, R28 and R45, are analyzed. For both runs selected the surface velocity components show prominent spectral peaks in a frequency range at about 0.15 Hz, along with stable phases and high coherence. The dominant contribution to this range is found to be from the two lowest Rayleigh modes and the fundamental Love mode, approaching from a relatively narrow directional interval.

The transfer coefficient estimates are reproduced in Figure 1. $R^{(n)}$ and $L^{(n)}$ represent $E^{(n)}$ for Rayleigh and Love waves. It should be noted that the onset of $R^{(1)}$ does not correspond to the cutoff frequency, which is below the analysis interval, but coincides with an abrupt increase of the transfer function. Figure 2 gives the directional estimate $\sigma(\theta)$, compared to the directions of approach observed.

Simultaneously with R28 and R45, NORSAR (Norwegian Seismic Array) wave number spectra were recorded for frequencies 0.14 Hz and 0.15 Hz (Figure 3).

The wave directions in Figure 2 and Figure 3 are drawn with reference to the recording location in the geographical maps of Figures 4 and 5. In the case of R28, the directional data from Sylt and NORSAR are consistent with one dominant source. In the case of R45, the NORSAR data imply contributions from separate sources of comparable strength. They are not resolved in the Sylt data, but are obviously responsible for the broader beam width of R45 compared to that of R28.

In the following, R28 only is considered for

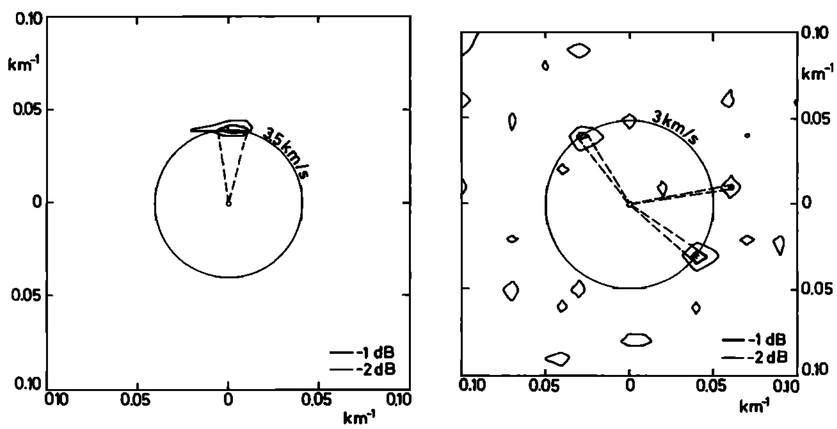

Fig. 3. NORSAR wave number spectra at 0.14 Hz (left) and at 0.15 Hz (right), corresponding to R28 and R45. The point marked with a cross is at zero dB, contours are at -1 dB and -2 dB. The aperture of the -1 dB contour enters into the geographical maps of Figures 4 and 5 as angle of incidence of substantial microseismic surface wave energy. (The spectra were kindly made available by H. Bungum).

source spectrum estimates. In this case, the waves are close to unidirectional, hence equation (7)--for $\sigma(\theta) \approx \delta(\theta - \bar{\theta})$, where δ = Dirac function, and $\bar{\theta}$ = mean direction--and equation (5) may be combined to yield

$$S(\underline{k}_n, -f) = \frac{\cos(\nu - \theta_r)}{(A/R)\cos(\nu - \theta)} \frac{c_s^{(n)} v_s^{(n)} v_r^{(n)} T_{e,r}^{(n)}}{2\pi f \, T_{e,s}^{(n)}} \cdot \exp\left[2\gamma^{(n)} R\right] E^{(n)} \tag{8}$$

where

$$T_e^{(n)} = T_1^{(n)} + T_2^{(n)} + T_3^{(n)}$$

Rayleigh Wave Source Area

During the 12 hours before the measurements of R28, the weather conditions were characterized by a pronounced low pressure system over the North Atlantic (Figures 6 and 7). The center of the depression propagated about 250 km in a northeasterly direction, which corresponds to an average velocity of 20 km/h; the wind velocities of the associated storm area amounted to about 60 km/h to 70 km/h. The atmospheric conditions allowed for effective generation of ocean waves directed toward the Norwegian coast.

Comparison of Figures 6 and 7 to Figure 4 shows

1. NORSAR microseisms approach from a direction where high-energy ocean waves affect the Norwegian coast.
2. The Sylt directions deviate from the corresponding coastal section, by roughly 10°, toward more easterly directions. The amount of deviation cannot be plausibly explained by lateral refraction or a systematic error due to the recording conditions. Rather, the Sylt data appear to be influenced by additional microseims from the Skagerrak. This follows from the considerable fetch with wind velocities of about 12 m/s to 16 m/s, directed toward Skagerrak's eastern coast. The doubled sea wave peak frequencies determined by these fetch conditions, however, lie well above the transfer coefficient peak frequencies. (Relationships between sea wave peak frequencies, wind velocity, and fetch are given later). The explanation is consistent with a directional frequency dependence.

Hence, the essential part of the Rayleigh wave component of R28 is attributed to ocean waves at the Norwegian coast roughly between 60°N and 70° N.

A number of authors have found the action of ocean waves at the Norwegian coast to be responsible for most of the European strong microseismic activity [Laska, 1902; Båth, 1952; Tams, 1953; Santô, 1962; Strobach, 1962; Bungum et al., 1971; Kulhánek and Båth, 1972; Schmalfeldt, 1978]. Actually, North Atlantic depressions directed toward the Norwegian coast are usually associated with large fetches (of up to more than 1000 km), giving rise to low-frequency and high-energy ocean waves.

Model of the Subsurface Structure

The structure of microseismic propagation is described in terms of horizontally stratified layered models for the source and recording areas.

The model of the recording area, adopted from paper 2, is given in Table 1. It is based upon the compressional (P) velocity structure known from seismic investigations. The shear (S) wave velocities of the crystalline basement are introduced according to Poisson's relation (Poisson's ratio equal to 0.25), and the densities according to the Nafe-Drake relation. The shear wave velocities of the younger sediments, which exert a strong influence mainly upon the horizontal wave components, are estimated as variable parameters in the inversion procedure.

The (Rayleigh wave) source area is situated on the Norwegian shelf. The near-coastal structure consists of crystalline bedrock running the whole length of the coast, and extending to between 10 km and 50 km from the coast. The source region, defined by coastally reflected ocean waves of appreciable energy (enabling effective ocean wave interaction) is considered to have

TABLE 1. Subsurface Layered Models Of The Recording Area (Upper Scheme) And Of The Rayleigh Wave Source Area (Lower Scheme)

Depth To Top Of Layer, km	Density, g cm^{-3}	P Wave Velocity, km s^{-1}	S Wave Velocity, km s^{-1}	Poisson's ratio
0.0	2.0	1.9	0.80	0.39
0.7	2.2	3.0	1.50	0.33
1.9	2.5	4.1	2.20	0.30
2.9	2.6	4.8	2.65	0.28
3.7	2.8	6.0	3.46	0.25
10.7	3.0	6.6	3.81	0.25
30.7	3.3	8.1	4.68	0.25
0.0	1.0	1.5	0.00	0.50
0.1	2.6	5.0	2.75	0.28
7.1	2.8	6.0	3.45	0.25
11.1	2.9	6.51	3.75	0.25
29.1	3.3	8.05	4.65	0.25

about the same normal-to-coast extension as the crystalline province. Few seismic investigations concerning the shallow subsurface structure of the near-coastal area are known. The works of Eldholm [1970] and Sellevoll [1975] reveal a typical near-surface P wave velocity of 5 km/s and only slightly higher values (about 5.5 km/s) at depths of about 5 km to 7 km. On these grounds, the source area is modeled as shown in Table 1. The Precambrian compressional structure at depths deeper than 7 km is extrapolated from the adjacent mainland. Shear wave velocities and densities are represented by typical values.

In broad outline, the structure between source and recording areas consists of folded Caledonian and Precambrian shield (region of Southern Norway) and a trough of substantial post-Palaeozoic sedimentation (near-coastal region of the Danish North Sea). The transition between consolidated and unconsolidated provinces occurring in the Skagerrak is characterized by a rather abrupt increase of the sedimentary coverage.

In the refractive model the range between source and recording areas is defined by a continuous transition zone.

Attenuation properties of surface waves for the period range considered (5-8 s) are scarce and have large uncertainties. Mitchell and Herrmann [1979] present quality factor data for both Rayleigh and Love waves (Q_R and Q_L) for the eastern USA. From earthquake-generated fundamental mode surface waves they obtain values of $Q_R^{(n=o)}$ and $Q_L^{(n=o)}$ between 250 and 400. In an earlier paper, Mitchell [1973] presents attenuation coefficient observations for fundamental and higher mode surface waves. They correspond to somewhat lower $Q_R^{(o)}$ and $Q_L^{(o)}$ values, $Q_R^{(1)}$ being slightly higher than $Q_R^{(o)}$.

The data are also taken to be typical for the structure under consideration. This conforms with Tryggvason [1965], who found consistent attenuation data for North America and Europe. Accordingly, quality factor estimates are given by $250 \lesssim Q_R^{(o)} \lesssim 400$; $300 \lesssim Q_R^{(1)} \lesssim 500$; and $150 \lesssim Q_L^{(o)} \lesssim 300$.

Source Spectrum Estimates From Rayleigh Wave Observations

Application of equation (8) is based upon two different subsurface models: (1) the Sylt model, so-called nonrefractive model (NRM), and (2) the refractive model (RM), defined in terms of the two layer systems of Table 1. A change in azimuth of the wave number vector during refraction is neglected ($\theta_r = \theta$). The ratio between source area and source distance is specified by A/R = 20 km, where R = 1200 km (Figure 4). The corresponding value of A is explained when the ocean wave field is considered.

Source spectra computed from $R^{(o)}$ and $R^{(1)}$ of R28 (Figure 1) are given in Figures 8a, 8b, and 8c for NRM and RM and different attenuation models. Obviously, the fundamental mode source spectra differ by relatively small amounts between the nonrefractive and the refractive model. On the other hand, the estimates from $R^{(1)}$, compared to those from $R^{(o)}$, are lower for NRM but higher for RM. According to theory, which predicts a wave number independent source spectrum, the fundamental and the higher mode observations should lead to coincident estimates. A possible coincidence would have to be discussed on the grounds of uncertainty intervals for the estimates. It can be said that the estimates from $R^{(1)}$, owing to their strong dependence upon the subsurface model, are much more uncertain

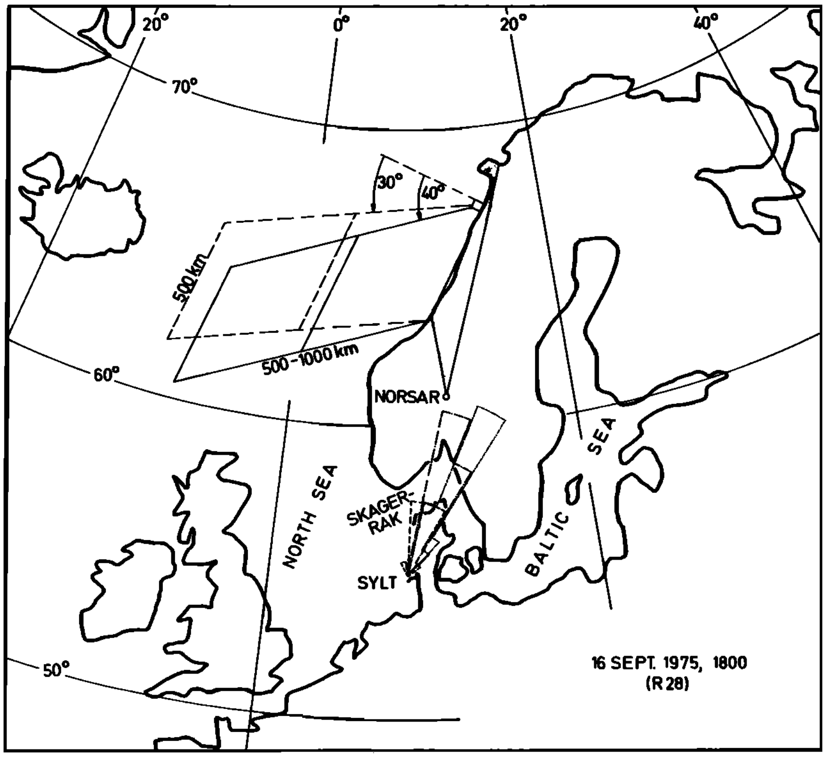

Fig. 4. Run R28. Directions of microseismic approach at Sylt array (Figure 2) and at NORSAR (Figure 3). Also, a schematic representation of the area of ocean surface wave generation is given. In the mapping, a straight line passing Sylt corresponds to a great-circle path (courtesy of J. Klußmann).

compared with the estimates from $R^{(o)}$. The model approximations suggest that the discrepancies between the source spectrum estimates are insignificant; hence the results do not contradict a wave number independent source spectrum.

Owing to their almost invariant behavior with respect to the subsurface model, the estimates from $R^{(o)}$ are considered to be reliable approximations to the actual source spectrum.

Remark: A comparison of the source spectra between subsurface models with and without attenuation reveals different spectrum slopings, the conservative model (vanishing attenuation) exhibiting the steepest frequency descent. The difference, particularly obvious in the fundamental mode spectra, results from the frequency-proportional energy loss. This demonstrates the effect of attenuation leading to a 'red shift' of the spectral components with decreasing Q and increasing R (definition of the attenuation coefficient according to equation (5)). Enhancement of surface wave periods with increasing source distance is well known from observations; it probably explains an observation by Rind [1980], who found the mean period of DF microseisms to be slightly higher than half the period of the generating ocean waves.

Ocean Wave Frequency Spectrum

The source spectrum estimates of Figure 8 suppose that Rayleigh waves may be generated by coastally reflected ocean waves. To test this hypothesis, the source spectrum is estimated from the generating ocean surface waves. The approach is based upon equation (2.15) of paper 1, which is an explicit relationship between directional ocean wave spectrum and (wave number independent) source spectrum.

The ocean wave spectrum is described in terms of model representations taken from sea wave generation research. Studies of wind wave growth [for example, Phillips, 1969] have revealed that spectra of waves generated by a reasonably uniform and steady wind typically show a steep forward face rising to a sharp maximum; at frequencies rather above that of the spectral maximum, they approach a form proportional to $g^2/(2\pi f)^5$, where g is gravitational acceleration. A characteristic frequency of the wave field is that of the spectral maximum ($f_m \approx g/2\pi u$) corresponding to components traveling at the wind speed u. The components with frequencies lower than f_m are still growing and, therefore, are unsaturated; the components above f_m are in equilibrium.

Frequency spectra of swell, defined to be a fully developed sea, have been described by various expressions of the type

$$\Phi(f) = \frac{g^2}{(2\pi f)^5} \phi(f/f_m) \tag{9}$$

A form most widely accepted is the 'Pierson-Moskowitz spectrum'

$$\Phi_{PM}(f;\ u) = 2\pi\alpha \frac{g^2}{(2\pi f)^5} \exp\left[-\frac{5}{4}(f/f_m)^{-4}\right] \tag{10}$$

where $f_m = 0.13$ g/u; u = wind speed at 10 m above

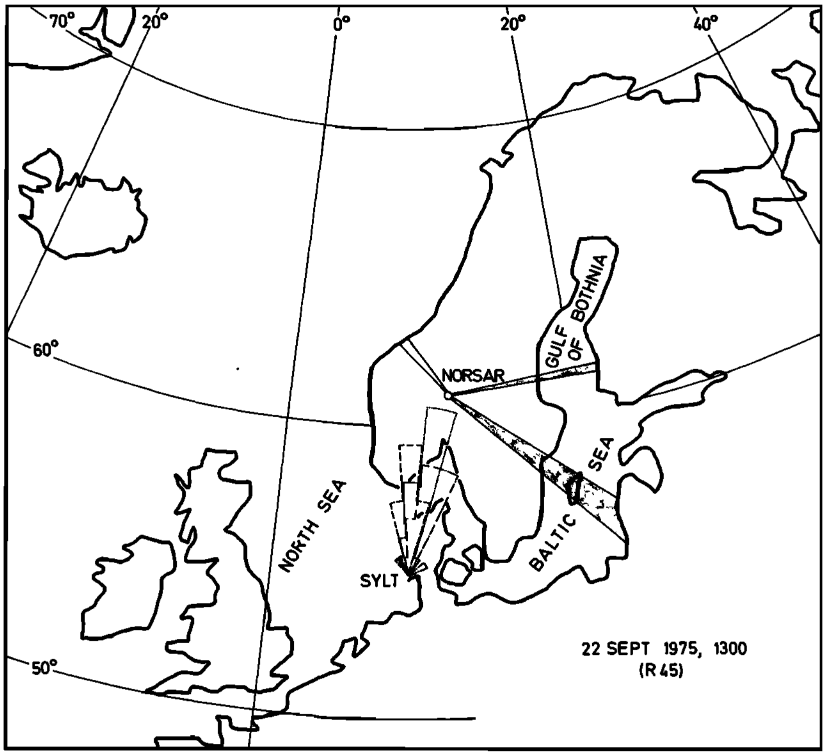

Fig. 5. Run R45; for legend, compare Figure 4.

the average wave height, and $\alpha = 0.0081$ (= Phillips' constant).

For high winds, the extent and duration of the uniform wind region may be insufficient to achieve a fully developed state. In these cases, the winds give rise to wind seas characterized by a fetch dependence of f_m and α through the nondimensional empirical expressions

$$\tilde{f}_m = 2.84\,\tilde{x}^{-0.3}$$
$$\alpha = 0.0662\,\tilde{x}^{-0.2} \qquad (11)$$

where $\tilde{f}_m = u\,f_m/g$, $\tilde{x} = g\,x/u^2$, and x = fetch, which is the linear extension, parallel to the wind direction, of the uniform wave-generating wind field [Hasselmann et al., 1976]. Equations (11) apply to nondimensional fetches below $\tilde{x}_o \approx$ 20,000 to 50,000 and nondimensional peak frequencies

$$\tilde{f}_m > \tilde{f}_o = 0.13 \qquad (12)$$

whereas $\tilde{f}_m = \tilde{f}_o$ for $\tilde{x} > \tilde{x}_o$ (swell range).

The spectral shape of a wind sea exhibits a narrower and more pronounced peak compared to the swell spectrum. A parametrical form established in an international wind wave growth experiment in the North Sea ('JONSWAP'), differs from equation (10) by an additional 'peak enhancement' factor, $\eta(f;\, f_m,\, \gamma,\, \sigma)$, defined by

$$\log_\gamma \eta = \exp\left[-\frac{1}{2}\left(\frac{f - f_m}{\sigma\, f_m}\right)^2\right] \qquad (13)$$

[Hasselmann et al., 1973]. If $\gamma \to 1$, then $\eta \to 1$, which means that the wind sea spectrum approaches the form of a swell spectrum.

The observed shape parameters γ or σ (actually, instead of σ two parameters σ_a and σ_b are considered for the left and right sided width of the spectral peak) do not reveal a fetch dependence. Their average values were compared with a number of spectra obtained from different experiments under a variety of generation conditions. Fitting a total of 333 spectra to the parameter model $p = p_o\, \nu^q$, where $\nu = \tilde{f}_m/0.251$, yielded

$$\gamma = 2.65\,\nu^{0.32} \pm 44\%$$
$$\sigma_a = 0.085\,\nu^{-0.32} \pm 76\% \qquad (14)$$
$$\sigma_b = 0.098\,\nu^{-0.16} \pm 47\%$$

the error intervals representing the average deviations of individual values from the regression values [Hasselmann et al., 1976].

Observed γ values, in general, are considerably higher than 1 for values of $\tilde{f}_m$ only slightly higher than $\tilde{f}_o$. This suggests that the transition of a wind sea spectrum to the fully developed spectrum occurs at a very final stage of development.

Rayleigh Wave Source Spectrum in Terms of the Directional Ocean Wave Spectrum

The near-coastal field of ocean surface waves, responsible for the generation of Rayleigh waves, is modeled upon the following conditions.

1. During 12 hours, roughly, before the microseismic measurements, fairly steady and uniform strong winds directed toward the Norwegian coast give rise to almost ideal ocean wave generation conditions. The corresponding fetch extending to the coast has dimensions of the

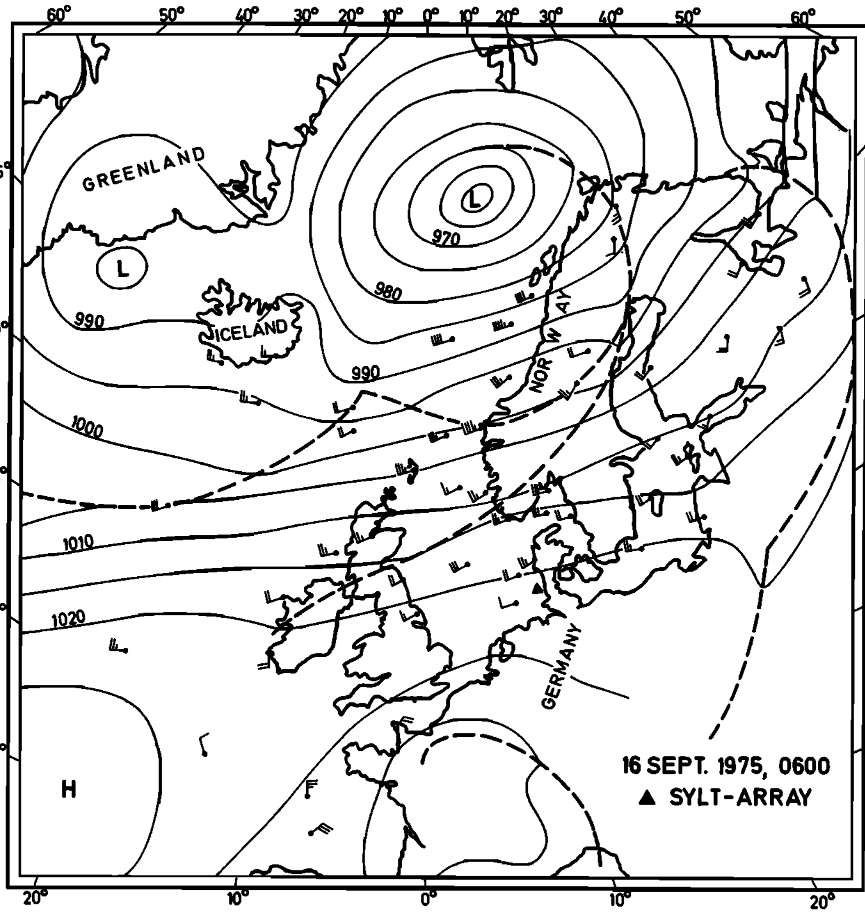

Fig. 6. R28. Surface weather chart 12 hours before the microseismic measurements. The atmospheric pressure field is represented by isobars at 5 mbar spacings. Wind velocities corresponding to the wind vectors may be read from Figure 9. (Deutscher Wetterdienst, Seewetteramt Hamburg).

order of 500 km to 1000 km and 400 km to 600 km in length and width. The wind velocities typically lie between 17 m/s and 21 m/s and the average wind direction ranges between 30° and 40° from the normal-to-coast direction (Figures 6 and 7 and Figure 4).

2. Within the area of ocean wave generation, the wave directions follow the frequency-independent equation

$$\tau(\theta;\bar{\theta}) = \begin{cases} \frac{2}{\pi}\cos^2(\theta-\bar{\theta}) & \text{for } |\theta-\bar{\theta}| \leq \frac{\pi}{2} \\ 0 & \text{otherwise} \end{cases} \tag{15}$$

where $\bar{\theta}$ = mean wind direction.

This formula is widely used in ocean wave forecasting problems.

3. The coastal section affected by the ocean waves is approximated by a steep plane, reflecting the wave energy independent of direction and frequency. The steep coast assumption implies that only deep-sea waves (defined by ratios between wavelength and water depth less than about 3) are considered, which may be justified by comparing the greatest wavelengths (370 m at 0.065 Hz) with the near-coastal water depths. On the other hand, a planar reflector highly idealizes the Norwegian coast fissured by fiords. The corresponding energy reflection coefficient is taken to be 0.2, which is a value obtained from swell recordings off the U.S. Pacific coast [Munk et al., 1963].

Consequently, the ocean waves propagating toward the coast are represented by the directional spectrum

$$\begin{aligned}\tilde{F}_\zeta(f,\theta) &= \Phi_{PM}(f;u,\alpha)\,\eta(f;f_m,\gamma,\sigma)\,\tau(\theta;\bar{\theta}) \\ &= P_\zeta(f)\,\tau(\theta;\bar{\theta})\end{aligned} \tag{16}$$

obtained by combining equations (10), (13), and (15).

The directional spectrum $\tilde{\tilde{F}}_r(f,\theta_r)$ of the coastally reflected waves differs from equation (16) by virtue of the directional distribution τ_r and an additional factor ε representing the coastal reflection coefficient. If θ is measured relative to the coastal normal, then $|\theta| \leq \pi/2$ and $\tau_r = \tau(\theta;-\bar{\theta})$. The coastal wave field is defined as a superposition of incident and reflected waves

$$\begin{aligned}F_\zeta(f,\theta) &= \tilde{F}_\zeta(f,\theta) + \tilde{\tilde{F}}_\zeta(f,\theta_r) \\ &= P_\zeta(f)\left[\tau(\theta;\bar{\theta}) + \varepsilon\,\tau(\theta;-\bar{\theta})\right]\end{aligned} \tag{17}$$

According to Hasselmann's concept [paper 1], oppositely traveling components give rise to a

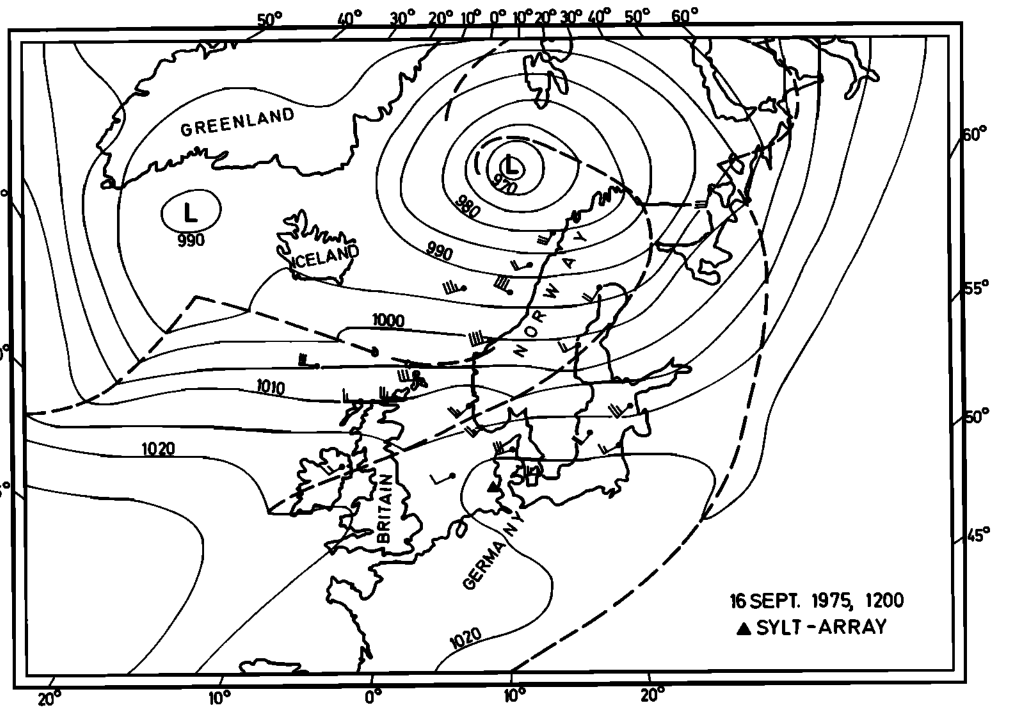

Fig. 7. R28. Surface weather chart 6 hours before the microseismic measurements.

pressure fluctuation at a frequency twice that of the component frequencies. In terms of specular reflection, corresponding wave components are confined to the interval $|\theta| \leqslant \pi/2 - |\bar{\theta}|$; hence the 'equivalent pressure spectrum' (= source spectrum), implying the component product integrated over all directions, reads (equation (18))

$$S_\zeta(f) = f/2 \left[\rho\ g\ P_\zeta(f/2)\right]^2 \epsilon \int_{-\pi/2+|\bar{\theta}|}^{\pi/2-|\bar{\theta}|} \tau(\theta;\ \bar{\theta})\ \tau(\theta;\ -\bar{\theta}) d\theta$$

where ρ is water density.

Source Spectrum Estimates From the Ocean Wave Model

Wind seas are principally characterized by their peak frequency. For example, peak frequency occurs as the relevant parameter in a 'wave prediction model' developed by Hasselmann et al. [1976]. The dependence of peak frequency upon wind velocity and fetch, given by the first of equations (11), is shown in Figure 9. The figure also displays the domain of the parameters determining the ocean wave generation conditions (hatched area) as inferred from the weather charts. It follows that the peak frequencies induced under these conditions, lie essentially between 0.07 Hz and 0.08 Hz.

Compared to the microseismic peak frequencies (see $R^{(o)}$ in Figure 1, or the corresponding estimates in Figure 8), a 1:2 relationship is obvious.

Remark: Figure 9 illustrates the inverse behavior of peak frequency with respect to wind velocity and fetch. Hence, surface waves, on waters exhibiting rather limited fetch conditions, are confined to higher frequencies. For example, Baltic Sea fetches are restricted mainly to about 200 km to 400 km for westerly winds. It implies that the dominant wave energies induced by the usually moderate winds lie well above 0.1 Hz. Consistent with this, microseisms from the Gulf of Bothnia or from the Baltic Sea are confined typically to frequencies higher than 0.3 Hz [Santô, 1962; Bungum et al., 1971; Kulhánek and Båth, 1972].

Rayleigh wave source spectra computed with equation (18) are shown in Figure 10. The hatched curves enclose the uncertainty range defined by wind velocities of between 17 m/s and 21 m/s, and fetches of between 500 km and 1000 km (Figure 9), and by mean wind directions varying between 30° and 40° relative to the coastal normal.

The peak shape parameters determined according to equations (14) do not differ significantly from their averages, $\gamma = 2.2$, and $\sigma_a \approx \sigma_b = 0.10 \equiv \sigma$, which are taken as fixed parameters. The continuous smooth curves of Figure 10 correspond to $f_m = 0.076$ Hz, represented by the bold line section of Figure 9. The sea wave peak frequency f_m is half the microseismic peak frequency defined by the maximum of a quadratic polynomial fitting the peak region of the preferred estimate from $R^{(o)}$ (RM, $Q_R = 300$; Figure 8c).

The source spectrum estimates from $R^{(o)}$ shown in Figure 10 are reproduced from Figures 8a and 8c. The range of their variations, as induced by the different subsurface models, provides a rough measure of the uncertainties involved in their estimation.

Obviously, the two approaches based upon equations (8) and (18) lead to consistent Rayleigh wave source spectrum estimates. This result is a strong support for the source mechanism assumed.

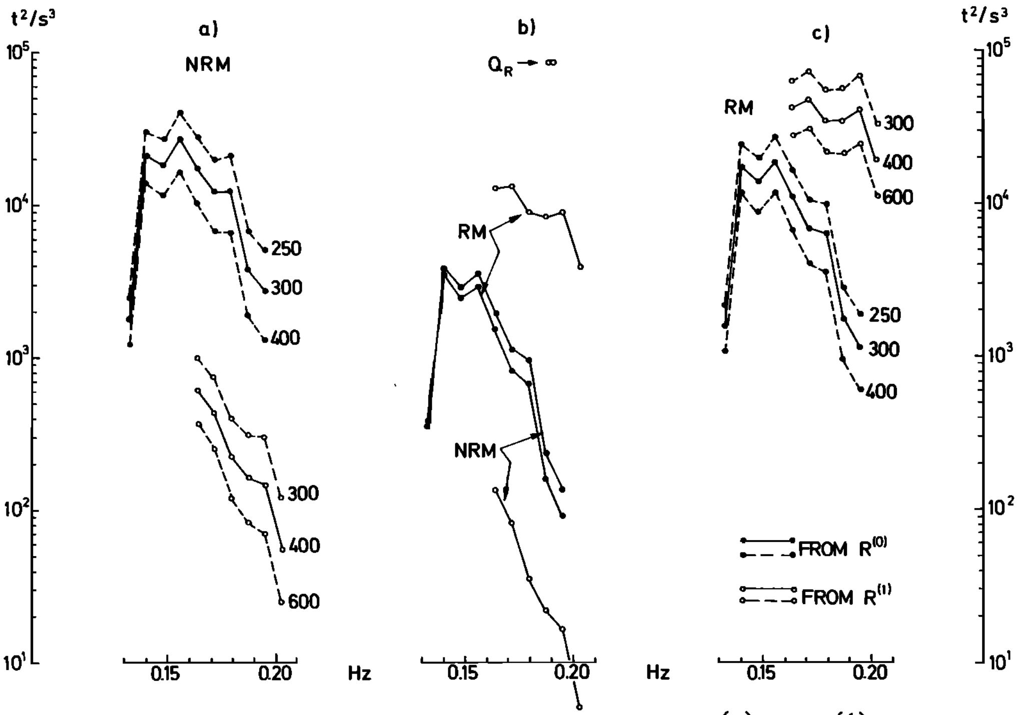

Fig. 8. R28. Rayleigh wave source spectra estimated from $R^{(o)}$ and $R^{(1)}$ (Figure 1) by using equation (8). Estimates are based upon the nonrefractive model (NRM) and the refractive model (RM), with different values of the quality factor.

Love Wave Component

To investigate the origin of the microseismic Love waves, some results from paper 2 concerning R28 are recapitulated.

1. Love waves and Rayleigh waves approach from the same directional interval (Figure 2).

2. The transfer coefficients of the fundamental Love and Rayleigh modes, $L^{(o)}$ and $R^{(o)}$ (Figure 1), show a high frequency-by-frequency correlation, which implies corresponding peak frequencies. The correlation coefficient between their logarithms is given by $0.57 \leqslant 0.90 \leqslant 0.98$, lower and upper limits defining a 95% confidence interval.

Remark: $L^{(o)}$ and $R^{(o)}$ of R45 exhibit a weaker resemblance. Most probably this is due to the influence of several sources appearing in R45.

The analogous appearance suggests a coupling between the two wave types. Possible explanations for the coupling are a common origin or a partial conversion of propagating Rayleigh waves into Love waves. So far, no theory explains microseismic Love waves.

Irrespective of a physical explanation, it is assumed here that (1) Love waves originate independently from the resonant action of a random stress field at the earth's surface, and (2) the 'equivalent stress spectrum' (= source spectrum) is approximately constant within a certain area sufficiently distant from the recording station and zero outside this area.

Hence equation (8) is applicable for Love wave source spectrum estimates from $L^{(o)}$.

Source spectra computed for coincident source areas of Love and Rayleigh waves serve to test the 'hypothesis of a common origin.' The rationale of this approach is that the correspondence between $L^{(o)}$ and $R^{(o)}$ is conditioned by the source(s) and, therefore, ought to be reflected in the source spectra, too.

Love wave source spectra estimated in analogy to the Rayleigh wave source spectra of Figure 8, are given in Figure 11. Figure 12c shows the ratio between $L^{(o)}$ and $R^{(o)}$ and, to illustrate

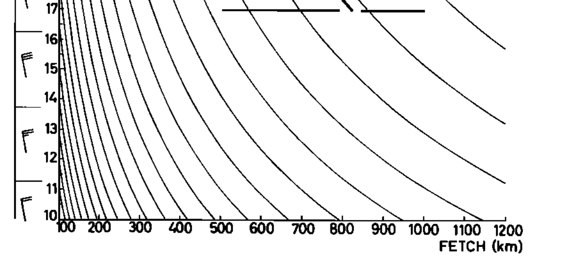

Fig. 9. Dependence between wind velocity, fetch, and peak frequency for wind seas developing under ideal generation conditions, given by the first of equations (11). Curves correspond to peak frequencies at 0.005 Hz spacings. The hatched area defines a range of uncertainty of wind velocity and fetch determining the ocean wave generation conditions for R28.

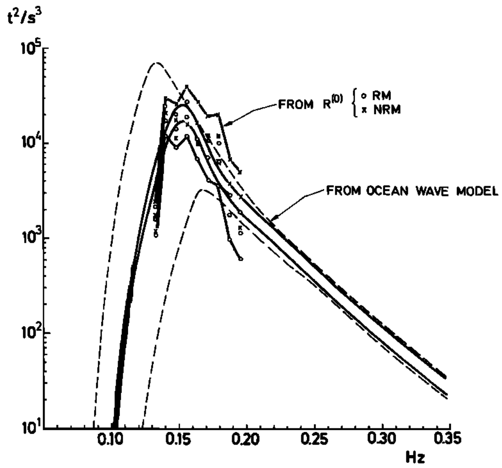

Fig. 10. Comparative source spectrum estimates based upon equations (8) and (18), respectively. The hatched curves enclose all spectra computed from the ocean wave model, for the domain defined in the text; the smooth curves correspond to a sea wave peak frequency of 0.076 Hz. The spectra estimated from $R^{(o)}$ are reproduced from Figures 8a and 8c.

the role of the local transfer functions, also the ratio between

$$P_{e,R} = \sum_{n=0}^{1} \sum_{i=1}^{3} P_{i,R}^{(n)} \tag{19a}$$

and

$$P_{e,L} = \sum_{i=1}^{2} P_{i,L}^{(o)} \tag{19b}$$

representing energy density of Rayleigh and Love waves, respectively.

Ratios between source spectra of Love waves ($= S_L$, from $L^{(o)}$) and Rayleigh waves ($= S_R$, from $R^{(o)}$) appear in Figure 12a. Except for the unrealistic conservative nonrefractive model, S_L/S_R exhibits a clear frequency dependence, which is not obvious from $L^{(o)}/R^{(o)}$. The transfer properties responsible for this behavior can be characterized by the dimensionless quantities

$$\phi = \frac{v_{r,R}^{(o)} v_{s,R}^{(o)} R^{(o)}}{S_R}$$
$$\psi = \frac{v_{r,L}^{(o)} v_{s,L}^{(o)} L^{(o)}}{S_L} \tag{20}$$

for Rayleigh and Love waves, respectively (see equation (8)). They are represented in Figure 12b. Accordingly, the dominant influence is due to Love wave attenuation. Realistic values of the quality factor imply a much stronger frequency dependence of ψ than of ϕ. In consequence, there is a much weaker correlation between $L^{(o)}$ and S_L than between $R^{(o)}$ and S_R, which in turn involves a lower correlation between S_L and S_R than between $L^{(o)}$ and $R^{(o)}$.

Particularly, the refractive Rayleigh wave model is distinguished by an almost frequency-independent ϕ, whereas the frequency trend of ψ

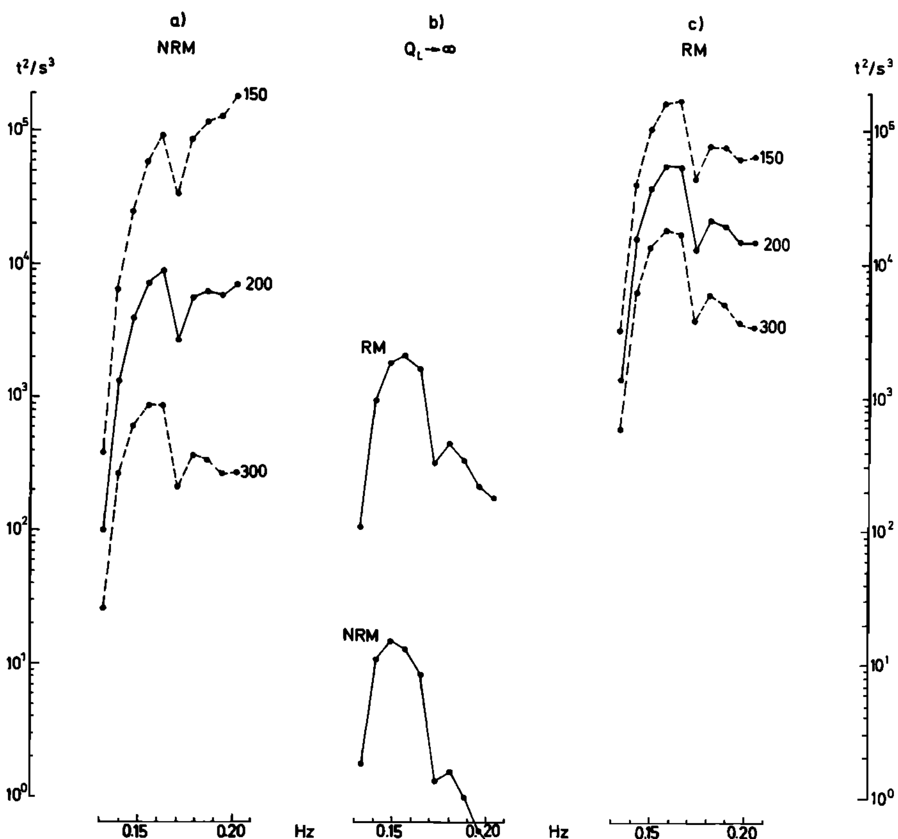

Fig. 11. R28. Love wave source spectra estimated from $L^{(o)}$ (Figure 1) by using equation (8).

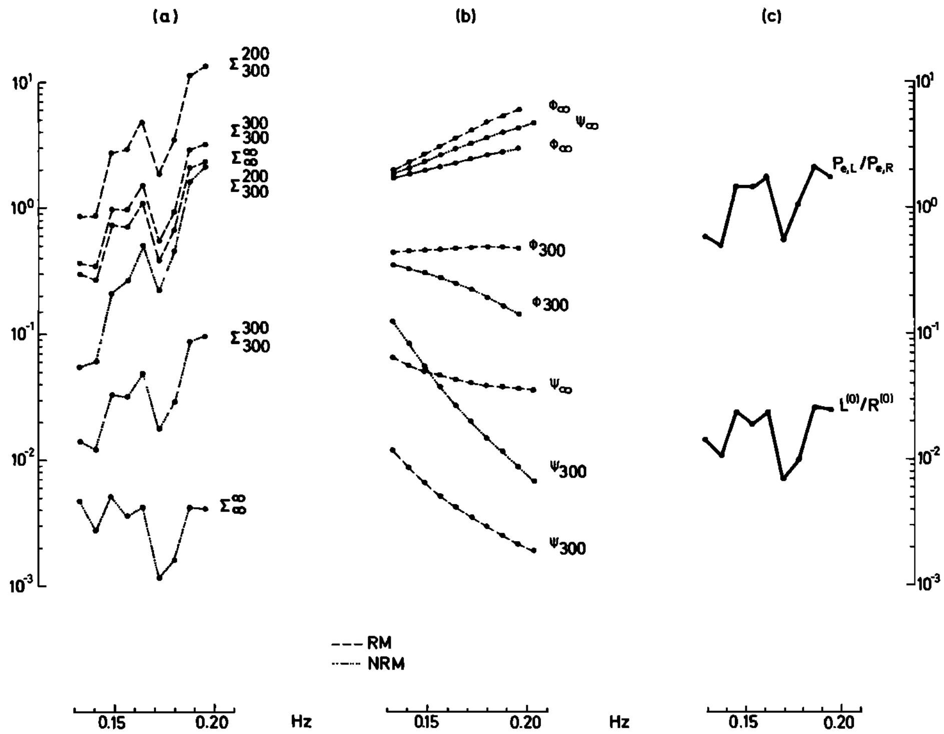

Fig. 12. R28. Nondimensional ratios, (a) between source spectra S_L and S_R, where $\sum\frac{Q_L}{Q_R} = S_L(Q_L) / S_R(Q_R)$, (b) between transfer coefficients and normalized source spectra, given by $\phi(Q_R)$ and $\psi(Q_L)$ (equation (20)), and (c) between energy densities $P_{e,L}$ and $P_{e,R}$ (equation (19)) and between transfer coefficients $L^{(o)}$ and $R^{(o)}$.

would only be reduced significantly for a less distant Love wave source. Hence a common origin of Love and Rayleigh waves is not consistent with the models considered.

There is another aspect concerning the physics of the problem. The peak frequency of S_L, corresponding to double the ocean wave peak frequency, would imply Love wave generation from a mechanism related to ocean wave interactions. However, pressure fluctuations resulting from the wave interactions cannot induce Love waves.

It must be emphasized that the Love waves are interpreted here in terms of one single source (analogous to Rayleigh waves), and also, the Love wave source spectrum estimates are based upon artificial assumptions; therefore, the inference remains rather speculative.

Conclusions

In this paper microseismic observations involving Rayleigh and Love wave components are interpreted in terms of source spectrum estimates.

The Rayleigh wave component is consistently explained by coastal reflection of ocean surface waves, which confirms the theoretical concept of Hasselmann [1963].

The Love wave component shows a coupling to the Rayleigh waves with respect to incidence directions and pattern of the 'transfer coefficients' about the peak frequency range. The source spectrum estimates contradict rather than support a common origin. A more reasonable explanation appears to be that microseismic Love waves are due to partial conversion of propagating Rayleigh waves.

DF microseisms in the frequency band considered (0.13 Hz to 0.17 Hz) originate typically from ocean areas where large wind fetches give rise to ocean surface waves at correspondingly low frequencies (0.06 Hz to 0.09 Hz). The usually high microseismic energies, and also the well-known increase of energy with increasing period [Hardtwig, 1949; Gutenberg, 1958], are a direct consequence of the (almost quadratic) dependence of the Rayleigh wave source spectrum on the ocean wave frequency spectrum.

Acknowledgments. The author is greatly indebted to Dorothee von Berg for extensive computer programming work. The research was supported by the Sonderforschungsbereich 94, Meeresforschung Hamburg, sponsored by the Deutsche Forschungsgemeinschaft.

References

Banerji, S. K., Microseisms associated with disturbed weather in the Indian Seas, Philos. Trans. R. Soc. London Ser. A, 229, 287-328, 1930.

Bath, M., An investigation of the Uppsala microseisms, Medd. Meteorol. Inst. Uppsala, 14, 168 pp., 1949.

Bath, M., Review over investigations of microseisms in Scandinavia, Pontif. Acad. Sci. Scr. Varia, 12, 239-276, 1952.

Bernard, P., Sur certaines propriétés de la houle étudiées a l'aide des enregistrements séismo-

graphiques, Bull. Inst. Océanogr. Monaco, 800, 1-19, 1941.
Bertelli, T., Osservazioni sui piccoli movimenti dei pendoli in relazione ad alcuni fenomeni meteorologiche, Boll. Meteorol. Osserv. Coll. Roma, 9, 10 pp., 1872.
Bungum, H., E. Rygg, and L. Bruland, Short-period seismic noise structure at the Norwegian Seismic Array, Bull. Seismol. Soc. Am., 61, 357-373, 1971.
Darbyshire, J., Identification of microseismic activity with sea waves, Proc. R. Soc. London Ser. A, 202, 439-448, 1950.
Darbyshire, J., and E. O. Okeke, A study of primary and secondary microseisms recorded in Anglesey, Geophys. J. R. Astron. Soc., 17, 63-92, 1969.
Eldholm, O., Seismic refraction measurements on the Norwegian continental shelf between 62°N and 65°N, Nor. Geol. Tidsskr., 50, 215-229, 1970.
Gherzi, E. S. J., Microseisms associated with storms, Gerlands Beitr. Geophys., 25, 145-147, 1930.
Gutenberg, B., Microseisms and weather forecasting, J. Meteorol., 4, 21-28, 1947.
Gutenberg, B., Microseisms, microbaroms, storms and waves in western North America, Eos Trans. AGU, 34, 161-173, 1953.
Gutenberg, B., Microseisms, Adv. Geophys., 5, 53-91, 1958.
Gutenberg, B., and H. Benioff, An investigation of microseisms, Final Rep. contract A.F.19(122) 436, Calif. Inst. of Technol., Pasadena, 1956.
Hardtwig, E., Die Mikroseismik und ihre Anwendung zum Abschätzen der Dicke der Kontinentalschollen, Geofis. Pura Appl., 14, 3-24, 1949.
Hasselmann, K., A statistical analysis of the generation of microseisms, Rev. Geophys. Space Phys., 1, 177-210, 1963.
Hasselmann, K., T. P. Barnett, E. Bouws, H. Carlson, D. E. Cartwright, K. Enke, J. A. Ewing, H. Gienapp, D. E. Hasselmann, P. Kruseman, A. Meerburg, P. Müller, D. J. Olbers, K. Richter, W. Sell, and H. Walden, Measurements of wind-wave growth and swell decay during the Joint North Sea Wave Project (JONSWAP), Ergänzungsheft Dtsch. Hydrogr. Z., A(12), 95 pp., 1973.
Hasselmann, K., D. B. Ross, P. Müller, and W. Sell, A parametrical wave prediction model, J. Phys. Oceanogr., 6, 200-228, 1976.
Haubrich, R. A., and K. McCamy, Microseisms: Coastal and Pelagic sources, Rev. Geophys. Space Phys., 7, 539-571, 1969.
Haubrich, R. A., W. H. Munk, and F. E. Snodgrass, Comparative spectra of microseisms and swell, Bull. Seismol. Soc. Am., 53, 27-37, 1963.
Hinde, B. J., and P. J. Gaunt, Some new techniques for recording and analyzing microseisms, Proc. R. Soc. London Ser. A, 290, 297-317, 1966.
Jung, K., Über mikroseismische Bodenunruhe und Brandung, Z. Geophys., 10, 325-329, 1934.
Kulhanek, O., and M. Bath, Power spectra and geographical distribution of short-period microseisms in Sweden, Pure Appl. Geophys., 94, 148-171, 1972.
Lacoss, R. T., E. J. Kelly, and M. N. Toksöz, Estimation of seismic noise structure using arrays, Geophysics, 34, 21-38, 1969.
Laska, W., Über die Pendelunruhe, Gerlands Beitr. Geophys. Ergänzungsband, 1, 209-235, 1902.
Longuet-Higgins, M. N., A theory of the origin of microseisms, Philos. Trans. R. Soc. London Ser. A, 243, 1-35, 1950.
Miche, M., Mouvements ondulatoires de la mer en profondeur constante ou décroissante, Ann. Ponts Chaussees, 114, 25-87, 131-164, 270-292, 396-406, 1944.
Mitchell, B. J., Surface-wave attenuation and crustal anelasticity in Central North America, Bull. Seismol. Soc. Am., 63, 1057-1071, 1973.
Mitchell, B. J., and R. B. Herrmann, Shear velocity structure in the Eastern United States from the inversion of surface-wave group and phase velocities, Bull. Seismol. Soc. Am., 69, 1133-1148, 1979.
Munk, W. H., G. R. Miller, F. E. Snodgrass, and N. F. Barber, Directional recording of swell from distant storms, Philos. Trans. R. Soc. London Ser. A, 255, 505, 1963.
Oliver, J., and M. Ewing, Microseisms in the 11 to 18 seconds period range, Bull. Seismol. Soc. Am., 47, 111-127, 1957.
Phillips, O. M., The Dynamics Of The Upper Ocean, Cambridge Monogr. on Mech. and Appl. Math., Cambridge University Press, 261 pp., 1969.
Press, F., and M. Ewing, A theory of microseisms with geological applications, Eos Trans. AGU, 29, 163-174, 1948.
Rind, D., Microseisms at Palisades, 3, Microseisms and microbaroms, J. Geophys. Res., 85, 4854-4862, 1980.
Santo, T. A., Energy sources of microseisms in Sweden, Ann. Geofis., 15, 335-377, 1962.
Schmalfeldt, B., Ein Vergleich von Mikroseismik- und Seegangsspektren und ein Versuch die Anfachungsgebiete zu lokalisieren, Hamb. Geophys. Einzelschr., 35, 53 pp., 1978.
Sellevoll, K., Seismic refraction measurements and continuous seismic profiling on the continental margin off Norway between 60°N and 69°N, Nor. Geol. Unders., 316, 219-235, 1975.
Strobach, K., Ein Beitrag zum Problem der Entstehung und der Wellennatur der mikroseismischen Bodenunruhe, Hamb. Geophys. Einzelschr., 5, 125 pp., 1962.
Szelwis, R., Inversion of microseismic array cross spectra, Bull. Seismol. Soc. Am., 70, 127-148, 1980.
Tams, E., Einige Korrelationen zwischen seismischer Bodenunruhe in Hamburg und der Brandung in West- und Nordeuropa, Z. Geophys., 9, 23-31, 1953.
Toksöz, M. N., and R. T. Lacoss, Microseisms: Mode structure and sources, Science, 159, 872-873, 1968.
Tryggvason, E., Dissipation of Rayleigh wave energy, J. Geophys. Res., 70, 1449-1455, 1965.
Wiechert, E., Verh.d.Zweiten Internat.Seismolog. Konf.Strassburg 1903, Gerlands Beitr. Geophys. Ergänzungsband, 2, 41, 1904.

(Received December 29, 1980;
revised January 13, 1982;
accepted April 9, 1982.)